Available online at www.sciencedirect.com
ScienceDirect
Journal of Sound and Vibration 313 (2008) 525–543
JOURNAL OF SOUND AND VIBRATION
www.elsevier.com/locate/jsvi

Recovery of elastic parameters of cellular materials by inversion of vibrational data

Erick Ogam[a,1,*], Armand Wirgin[a,1], Stefan Schneider[a], Z.E.A. Fellah[a,1], Yongzhi Xu[b,1]

[a]CNRS Laboratoire de Mécanique et d'Acoustique UPR7051, 31 chemin Joseph Aiguier, 13402 Marseille Cedex 20, France
[b]Department of Mathematics University of Louisville, KY 40292, USA

Received 21 October 2006; received in revised form 20 November 2007; accepted 21 November 2007
Available online 4 January 2008

Abstract

This investigation addresses the inverse problem of the retrieval of the macroscopic Young's modulus and Poisson ratio of light fluid-saturated cellular materials from the measured resonance frequencies of their vibrational response. The latter is shown to be generally nonlinear for all except very small excitations. In order to remain in the linear regime, and thus avoid ambiguities in the characterization of the material, we employ lightweight piezoelectric transducers and sensors and a low-noise amplifier for the acquisition of dynamic response data. The cellular materials under investigation (polyurethane, melamine) are shown to behave as isotropic, (equivalent) homogeneous elastic solids with Rayleigh damping (equivalent to a rheological model having the same dependence of attenuation on frequency) in the frequency band of interest. Our viscoelastic model is validated by comparing its predictions of the dynamic response of the specimens to the predictions of the more complete Biot interaction model. The computations with both of these models are carried out by means of 3D finite element (FE) codes for a variety of specimen shapes and sizes. Once the simpler viscoelastic model is validated, it is then employed to compute the trial resonance frequencies (which are the solutions of an eigenvalue problem associated with this model) during the inversion process. The cost function, which is a measure of the discrepancy between the trial and measured resonance frequencies for a number of vibrational modes, is constructed and then minimized by the Levenberg–Marquardt optimization algorithm in order to recover the sought-for moduli. Finally, a discussion is presented concerning the influence of the size and shape of the specimens, as well as the number of employed modes, on the uniqueness and quality of the inversion.

1. Introduction

The purpose of this work is to develop an experimental data-acquisition technique and inversion scheme for recovering the macroscopic elastic moduli and damping factors of specimens of arbitrary shape and size, composed of cellular materials.

*Corresponding author. Tel.: +33 4 91 16 44 82; fax: +33 4 91 16 42 70.
E-mail address: ogam@lma.cnrs-mrs.fr (E. Ogam).
[1]Work done within the framework of Action CNRS/Etats-Unis 2005-2007: Caractérisation vibroacoustique de l'os: aspects fondamentaux et applications au diagnostic et au suivi du traitement de l'ostéoporose.

0022-460X/$ - see front matter © 2007 Elsevier Ltd. All rights reserved.
doi:10.1016/j.jsv.2007.11.052

To do this, we employ an inversion method, used in the past (e.g., Refs. [1,2]) to characterize dense homogeneous (such as metals) or inhomogeneous (such as composites) solid specimens, whereby the processed data concern the relatively low resonance frequencies (<3 kHz) of various mechanical modes of the specimen. However, this method cannot be transposed to low-density cellular materials without precaution. In fact, the acquisition of data must be made in the linear response regime (which, for cellular materials, requires very small excitations, giving rise to very weak responses) and an appropriate model (incorporating as much as necessary, but not more, of the physics of the vibratory phenomena) must be employed in the inversion scheme to describe the (linear) dynamic response of the porous specimen.

This study is undertaken in the framework of the vibroacoustic characterization of bone for the detection of osteoporosis. When osteoporosis (which is an imbalance that results when bone resorption (the part of remodeling consisting of breaking down and assimilating) exceeds bone formation) sets in, bone becomes more fragile, with fewer connected and thinner trabeculae (in the form of rods and plates), and more porous cortical components. It has been demonstrated that the elastic and shear moduli (obtained by static mechanical tensile and torsional testing) of human femoral cortical bone in the longitudinal direction decrease significantly with the porosity (assessed by means of histology) [3]. Our aim is ultimately to employ the tool developed herein (which applies to specimens in their natural size and shape, contrary to other tools [4–7] which require the specimen to be cut into specific shapes in order to benefit from the existence of simple interaction models for these shapes) to establish a quantitative correlation (if it exists) between the macroscopic elastic moduli of bones having various porosities and their resistance to fracture.

Cancellous (also called trabecular) bone is the principal component of short bones such as vertebrae and is also found at the extremities of long bones (proximal tibia and femur) where it is surrounded by a shell of dense compact (cortical) bone. The mechanical behavior of cancellous bone is typically that of a cellular material. For instance, the compressive stress–strain curve is divided into three regimes characteristic of all cellular solids, and the moduli and strength all vary with density in the way expected of a foam [8]. Cancellous bone supports large static and cyclic loads.

Foaming materials (e.g., metals and polymers) into cellular solids, made up of an interconnected network of solid struts (rods) or plates, augments their mechanical properties, making them attractive for energy-absorbing applications. The techniques used for foaming are well documented in Ref. [8].

Cellular materials are poroelastic (or poroviscoelastic), so that their vibroacoustic behavior can be modeled by the Biot theory [9,10]. This theory, which assumes the solid phase to be saturated by a fluid phase, takes into account the motions of both the solid frame and the pore fluid, as well as their relative motions (which is the cause of viscous losses) [11,12]. The poroelastic material is described by five geometrical parameters (the porosity ϕ, flow resistivity σ^{fr}, tortuosity α_∞, viscous characteristic length Λ, thermal characteristic length Λ') and by the mechanical parameters of the frame and fluid. Recovering all these parameters by inversion of the measured acoustic waves propagating through the fluid in the pores, and through the elastic stress waves carried through the solid frame of the material, is a possible, but necessarily difficult task. It can be done using the Biot theory, or, perhaps, with the somewhat simpler Attenborough [13] and Allard [14] models. Another approach is to consider several of the parameters to be known a priori, and to invert the data for the other parameters via the Biot [15,16], Biot–Johnson–Champoux–Allard [5], and Johnson–Champoux–Allard (for rigid-frame porous materials, also known as equivalent fluid [17]) models. But all of these models are very expensive in terms of computational cost and memory and the data are either not sensitive to variations of certain parameters, and/or it may not be necessary to search for many of these parameters as such if their effect on the strength (or other property) of the material is either negligible or is globalized in the effective elastic moduli (or wavespeeds and attenuation factors) of the specimen.

This may explain why simple, relaxational, models for the acoustical properties of porous media (these are phenomenological models for sound propagation) which involve just a few parameters have been so popular. An extreme example of these simple models includes the empirical equations of Delany and Bazley [18,19] with just one adjustable parameter, the flow resistivity σ^{fr}.

Fairly comprehensive studies of the influence of the Biot–Johnson–Champoux–Allard model parameters on ultrasonic wave propagation in plate-like specimens of human cancellous bone, as well as methods for solving the inverse problem, have been reported by several authors [5,15,20,21]. It should be noted, in connection with carrying out a similar study using vibrational data, that the resonance frequencies and damping

(the observables) of vibrating cellular structures not only depend on their elastic moduli and geometrical parameters but also strongly on the size and shape of the specimen (also, unfortunately, on the boundary conditions).

In a study of the solid frame for relatively rigid materials, taking into account the sole inertial interactions, an approximate calculation of the resonance frequencies of a *porous plate* has been proposed and the influences of porosity, tortuosity and permeability have been studied in Ref. [22]. It was found that the natural frequency of the dominant mode increases with increasing porosity and permeability, and decreases with increasing tortuosity, whereas the damping factor increases with increasing porosity and decreases with increasing tortuosity, while reaching a maximum value at a frequency determined by the three parameters.

Notwithstanding these facts, it is tempting (and certainly useful, in the inverse problem context) to bypass completely models employing geometrical parameters such as porosity and tortuosity, and to incorporate their effect, in a homogenized way, into the elastic moduli (considered to be complex, in order to take into account dissipation of energy). This amounts to replacing the rather complicated Biot-like models by an elastic or modified elastic model incorporating damping effects (which we term the viscoelastic model herein). But in order for this to be legitimate, in the sense that it does not entail large errors in the reconstructed parameters of interest, we must first show (in the direct problem context) that the (simpler) viscoelastic model gives rise to a vibrational response that is close to that of the (more comprehensive) Biot-like model.

Thus, this paper starts with a description, in Section 2, of the experimental setup we use to acquire the vibration data (which constitutes the input to the inversion scheme). In Section 3 we present, and compare, the Biot–Johnson–Champoux–Allard model (BJCAM) and viscoelastic models (and their 3D, FE implementation schemes). The Rayleigh damping device employed in the viscoelastic model is related to a rheological model in this section. The good agreement between the BJCAM and viscoelastic models allows us to employ the simpler viscoelastic model in the inversion scheme also described in Section 3. The results and discussion are given in Section 4. The conclusions are given in Section 5.

2. The experimental setup for data acquisition

The experimental setup is designed for the acquisition of vibrational response data, in particular the resonance frequencies and spectra, that constitute the input to the inversion scheme for the recovery of the Young's modulus, Poisson ratio and damping factors of the cellular material.

Most of the methods that have been employed until now for characterizing cellular (and other) materials have often employed electromechanical shakers, accelerometers and laser vibrometry [23,24]. These devices are unwieldy, and/or expensive, and/or are not particularly well adapted to specimens with uneven, porous boundaries such as foams.

For this reason we chose to excite, and measure the motion of, the surface of the cellular material, with a minimum mass-loading effect on the structure, by means of a small (1.0 cm diameter), light-weight (0.11 g) axial piezoelectric transducer (PZT) and a similar sensor, both made of a thin disc of piezoelectric ceramic bonded to a thin metal diaphragm [25]. These devices are routinely incorporated into buzzers (Kingstate KPEG165) and telephone ringers (i.e small battery-powered equipment) to deliver high audible sound output from a small (milliwatt) energy input.

When the PZT sensor is bonded to a deforming vibrating surface, a mechanical deformation is induced in the polarized crystal (resulting from tension and twisting of the sensor) leading to the generation of an electric charge. The PZT sensor measures a deformation (strain) [26]. Likewise, when the PZT crystal is submitted to a modulated electrical excitation, it vibrates (and emits sound waves). The light weight, small size and flat structure form of the PZTs facilitate their mechanical fixation on cellular structures like foam, with negligible influence on their vibration responses as compared, for instance, to accelerometers. The apparent disadvantage of the PZT is that, as an exciter, it can deliver only small levels of vibrational inputs to the specimen, and as a sensor, it delivers only very small electrical outputs. As we shall see later, the low level of vibrational input it delivers is another good reason for employing PZT actuators, and the low output level can be compensated for by the use of suitable amplification devices.

The samples are suspended on a test rig using nylon threads (corresponding to free–free boundary conditions). The exciter and sensor are bonded (using a thin double-sided scotch tape) laterally onto the

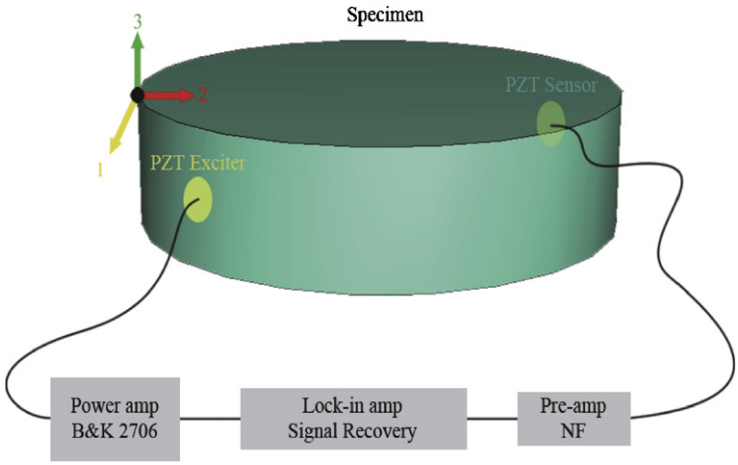

Fig. 1. The experimental setup.

specimen, opposite each other, as depicted in Fig. 1. The scotch is cut exactly to the size of the PZT discs to limit the introduction of extra damping effects into the measurements.

The exciter is driven in discrete frequency and amplitude steps using a Signal Recovery 7265DSP programmable lock-in oscillator and a Brüel and Kjær (B&K2706) power amplifier (Fig. 1). The response signal captured by the sensor is amplified using an NF SA-200F3 low-noise preamplifier connected to the input of a 7265DSP synchronous demodulator. The data from the amplifier are directly read by a PC via an HPIB (IEEE 488) bus.

The first two specimens (named PE1 and PE2) are disc-shaped (10 cm diameter, 2 cm thickness), cut from two different samples of melamine foam as is practiced for the characterization of the acoustic parameters of absorbing materials in an (e.g., B&K4002) impedance tube.

The third specimen (PE3) was cut into the form of a square (7 cm × 7 cm) thick plate (5 cm thickness) from the same panel as PE1.

Melamine, a strong organic base with the chemical formula $C_3H_6N_6$, is foamed into a micro-fibrous structure, resulting in an open cell material. It has become the standard synthetic vitreous fiber (SVF) material for sound absorption in anechoic chambers (such as the one at the Laboratoire de Mécanique d'Acoustique). Previously, the SVF were manufactured mostly from glass, natural rocks, slag and kaolin clay. These materials are still employed as insulation wools.

The fourth specimen (PE4) is made of polyurethane and was precisely cut into a thick, short hollow cylinder (8 cm exterior diameter, 6.5 cm interior diameter, 4 cm longitudinal dimension).

Other characteristics of the samples are given in Table 1.

The response spectra are measured from 100 Hz (just below the first resonance frequency of the specimens) up to 3 kHz.

2.1. Nonlinear behavior of the specimens

Evidence from our experiments (and elsewhere; see e.g., Refs. [27,28]) shows that cellular specimens exhibit nonlinear behavior. This is demonstrated by plotting their vibratory response as a function of the amplitude of excitation [29].

Four spectral responses of sample PE1 were measured by employing variable excitation amplitude voltage levels (0.02, 0.04, 0.06 and 0.08 V), applied to the transducer. The curves depicting the amplitudes and phases for the different levels of excitation are plotted in Fig. 2. The shift in the resonance frequencies with the increase in the level of excitation is more noticeable in the phase plot. The resonance frequencies shift downwards as the excitation amplitude is increased.

The inversions were done with data generated from the *lowest amplitude of excitation*, corresponding to a linear response of the specimens. These data had sufficient signal to noise ratios due to the use of the

Table 1
The density calculated from the measured weights (employing a Sartorius L2200S balance) and calculated volumes of the disc-shaped samples (diameter, 10.0 cm)

Specimen	Form	Thickness (cm)	Density ($kg\,m^{-3}$)
PE1	Thick disc	2.9	8.34
PE2	Thick disc	3.1	8.3
PE3	Thick plate	–	8.3
PE4	Hollow cylinder	1.5	32

Note that PE1 and PE2 are cut from different samples. The hollow cylinder has an exterior diameter of 8.0 cm and a height of 4.0 cm.

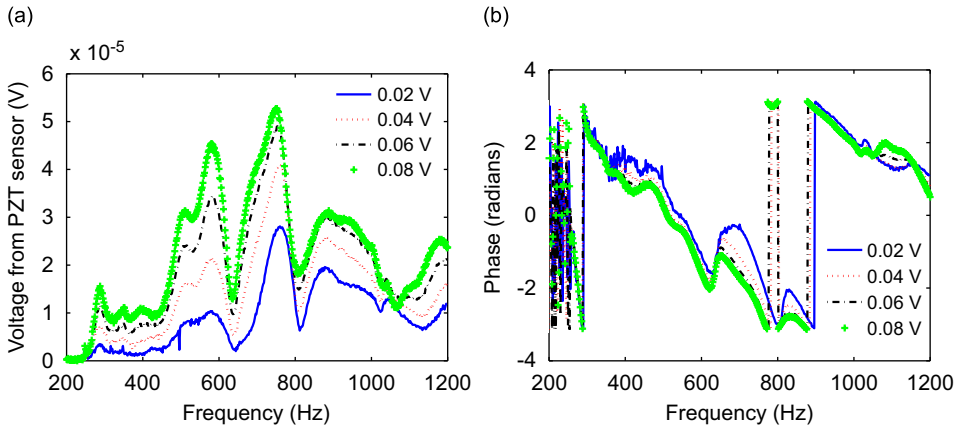

Fig. 2. The nonlinearities of the response (shift of resonance frequency with the variation of excitation amplitude) of specimen PE1: (a) the amplitude at different excitation voltages and (b) the phase.

high-sensitivity PZT sensors in association with a very low-noise amplifier connected to a synchronous demodulator/detection system.

3. Ingredients of the method for the recovery of the elastic moduli and damping factors of the specimens

3.1. Preliminary remarks

Most schemes for solving inverse problems (such as that of the recovery of the constitutive parameters of a specimen) proceed by solving the associated direct problem for a succession of trial values of the parameters of the configuration. This process is iterative and designed so that the successive trial values converge to the hopefully correct parameters of the configuration one wishes to characterize.

These schemes thus have three key ingredients: (i) the data constituting the response of the specimen to a known excitation, (ii) the model used to solve the aforementioned successive direct problems and (iii) the scheme for adjusting the successive values of the trial parameters so as to minimize the cost function.

3.2. Models for solving the direct problem

From the previous remarks, it can easily be appreciated that the choice of model for solving the direct problem is a key issue in that the numerical code stemming from this model will be used many (e.g., hundreds of) times during the iterative process involved in the resolution of the inverse problem. This model must therefore be as simple as possible (to speed up each resolution of the direct problem), while incorporating as much as possible of the physics of the most noticeable phenomena caused by the excitation of the specimen. This contradiction can only be resolved by a compromise.

As mentioned in the introduction, we have identified two candidate models for solving the direct problem. The first one is less costly in computation time and is the one actually employed for solving the inverse problem. The second one incorporates more of the physics, but, of course, requires intensive computations and is used only for the validation of the first model.

3.2.1. The first (viscoelastic) model

The specimen is initially visualized as a linear, isotropic elastic solid 3D body of arbitrary shape, attached to its environment by some sort of (we choose the free–free) boundary condition, and submitted to some sort of time-varying excitation. The microscopic irregularities and biphasic nature of the original porous medium are not explicitly taken into account; i.e., the medium is thought of as being homogenized on the scale of the micro-irregularities (but macro-irregularities can be accounted: for by the 3D geometrical model).

The body vibrates in response to the excitation and this phenomenon is described by the classical equations of the elastodynamics of continuous elastic media. Dissipation in the body is then accounted for by the introduction of Rayleigh damping.

The integral version of the governing partial differential equations (PDEs), which takes the form of the principle of virtual work expressed in Appendix A, is discretized so as to lead to

$$\delta\underline{u}^n\{M^{nm}\ddot{\underline{u}}^m + (C^{nm}_{(M)} + C^{nm}_{(K)})\dot{\underline{u}}^m + K^{nm}\underline{u}^m - P^n\} = 0, \tag{1}$$

wherein $\delta\underline{u}^n$ is the displacement variation, $m = 1, 2\ldots$, $n = 1, 2\ldots$, M^{nm}, K^{nm} are the mass and stiffness matrices, respectively, $C^{nm}_{(M)}$ and $C^{nm}_{(K)}$ the mass and stiffness viscous damping matrices, respectively, and P^n the external load vector. The displacement, velocity and acceleration are given by $\underline{u}^m$, $\dot{\underline{u}}^m$ and $\ddot{\underline{u}}^m$, respectively. Eq. (1) is the basis of the 3D finite element (FEM) implementation of the viscoelastic or elastic (for zero damping) models.

In order to compute the resonance frequencies, the damping matrices and the applied force are set to zero in Eq. (1). The eigenvalue problem for the natural modes is then to solve

$$(\lambda^2_{\text{eig}}M^{mn} + K^{mn})\phi^n = 0, \tag{2}$$

with λ_{eig} being the eigenvalue and ϕ^n the eigenvector (i.e., the mode of vibration).

As will be explained in more detail further on, the necessity of solving the eigenvalue problem makes itself felt in the inversion process, during which a subset of the natural frequencies, arising from a computation involving trial values of the elastic moduli of the specimen, is compared to the measured resonance frequencies.

A simple (Rayleigh damping) method is employed to account for the dissipation in the specimen, and manifests itself by the equivalent damping C_{eq} term appearing in Eq. (1). More specifically, Rayleigh damping is expressed by

$$C_{\text{eq}} = C^{nm}_{(M)} + C^{nm}_{(K)} = \alpha M^{nm} + \beta K^{nm}, \tag{3}$$

where α and β are constants (characteristics of the material, which, like the elastic moduli, will also be identified).

It can be shown that the damping ratio ξ_n of system (1), with assumption (3), is the following function of natural frequencies ω_n [30]:

$$\xi_n = \frac{\alpha}{2\omega_n} + \frac{\beta\omega_n}{2}. \tag{4}$$

Rayleigh damping can be related to the standard linear solid equation having a similar dissipative behavior. The creep function and the dissipative behavior of materials are described by using the viscoelastic constitutive equations originating in models composed of weightless springs (no inertial effects are present) and dash-pots (consisting of loosely fitting pistons in cylinders filled with a viscous fluid) [31].

The rheological interpretation of Rayleigh damping, using a particular generalized Maxwell (GM) model (Fig. 3), has been given in Ref. [32]. The equations relating α and β to the mechanical parameters of the GM

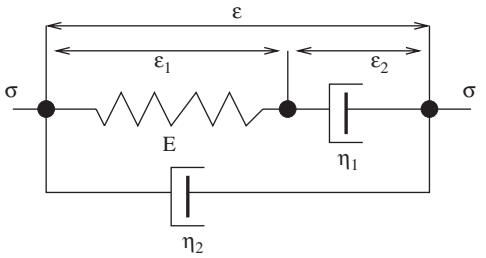

Fig. 3. The modified generalized Maxwell rheological model.

model are derived in Appendix B and are given by

$$\alpha = E(\eta_1 + \eta_2)/\eta_1^2, \quad \beta = \frac{\eta_2}{E}. \tag{5}$$

Dissipation can be quantified by using the quality factor Q. Its inverse Q^{-1} is the dissipation factor. The quality factor is also defined as twice the time-averaged strain energy density ($\langle V \rangle$) divided by the time-averaged dissipated energy density ($\langle D \rangle$) [31] ($Q = 2\langle V \rangle / \langle D \rangle$). The dependence of Q_{GM}^{-1} on frequency is then

$$Q_{\mathrm{GM}}^{-1} = \frac{E(\eta_1 + \eta_2)}{\eta_1^2 \omega} + \frac{\eta_2}{E}\omega. \tag{6}$$

The frequency response, for a point-like harmonic force applied to the specimen, is computed using Eq. (1) after the mechanical parameters have been recovered by inverting the measured resonant frequency data with the help of the model given by Eq. (2).

As explained more fully further on, this response is compared to the experimental spectral response to obtain the optimal values of α and β.

The numerical code associated with the 3D FE (visco) elastic model(s) is constructed with the help of a commercial FE software (Abaqus).

Accurate resonance frequency data for thick plates can also be generated by employing the 3D Ritz analysis [33] or by the differential quadrature (DQ) method [34] for moderately thick plates. Since the computation cost and precision of the 3D FE model depend on the number of elements chosen, the tables provided in [33] were used to make an optimal choice of the number of elements for the 3D FE (visco) elastic computations.

3.2.2. The second (Biot) model

The Biot model differs from the previous one in that the porous nature of the material of the specimen is explicitly taken into account. In fact, the medium is considered to have two components: the (elastic) solid frame (replaced by a homogenized solid) and the saturating fluid. The motions of these two components are described by a coupled system of PDEs. This coupling shows up notably in what appears as a viscous damping term which vanishes for vanishing relative motion of the two components and a volumetric coupling term.

In the $\{\underline{u}, p\}$ frequency domain formulation of the Biot theory formulated by Atalla [35], the mean displacement field $\underline{u}$ of the frame and the mean sound pressure p in the fluid phase over a homogenization volume are the variables of interest. The variational formulation of the governing differential equations is given in Appendix C. Eqs. (C.1) and (C.2) are the basis for the FE implementation of the Atalla–Biot model. Tilded variables therein are complex-valued, the imaginary parts of which represent dissipation effects in the material. Each of the nodes of the FE mesh has four degrees of freedom. Eqs. (C.1) and (C.2) are discretized using piecewise hierarchic polynomials as basis functions. The resulting sparse symmetric system of linear equations is solved, for each frequency, using a sparse direct solver.

3.2.3. Comparison of the two models

We employed the Biot model, implemented in our numerical code constructed from the formulation explained in Section 3.2.2, to generate reference solutions, concerning the response at a point on the surface of

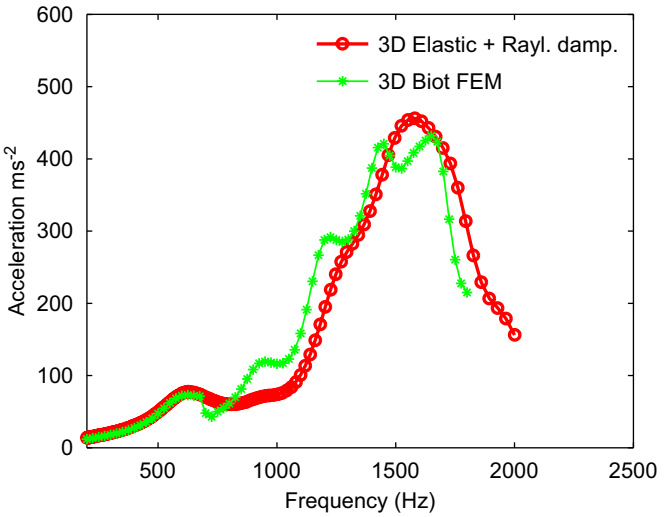

Fig. 4. Computed acceleration responses on a point of the surface of a 2.5 cm thick melamine disc specimen to a harmonic point force applied at another point of the surface, obtained by: (i) the viscoelastic FEM model incorporating Rayleigh damping parameters $\alpha = 1200$ and $\beta = 1 \times 10^{-6}$ and (ii) the Biot FEM model ($\phi = 0.97$, $\alpha_\infty = 1.015$, $\Lambda = 99\,\mu m$).

a 2.5 cm thick, melamine disc specimen to an applied concentrated force of 1 N at a point opposite to the first one on the disc surface. The nodal force acting on the frame of the absorbing material models the mechanical excitation of the sample caused by the actuator. Seven thousand two hundred FEs were used, resulting in 133,000 unknowns. Each frequency took 3.5 h of computation time on the SGI Origin3800 computer of the Center for Information Services and High Performance Computing of the Technische Universität in Dresden, Germany. This computation required previous knowledge of Young's modulus and Poisson ratio which were taken to be $E = 160\,kPa$, $\nu = 0.4$, as well as the geometric parameters ($\phi = 0.97$, $\alpha_\infty = 1.015$, $\Lambda = 99\,\mu m$, $\Lambda' = 283\,\mu m$), which were recovered from the inversion, with the help of the Johnson–Champoux–Allard model (equivalent fluid model [36]—the skeleton frame is considered motionless), of experimental acoustical reflection and transmission data [17] relative to the melamine disc excited by the waves radiated by 50, 100 and 200 kHz air-coupled ultrasonic transducers.

The 3D FEM (visco) elastic model, implemented by Abaqus software, was made to produce results, for the same specimen excited in the same manner. The specimen was discretized using 272 (1483 nodes) 20-node quadratic hexahedron brick elements (type C3D20R [37]). The total cpu time for the calculation of 128 frequencies (200–3 kHz) was 328 s on an Intel P4 3 GHz personal computer. This much shorter computation time constitutes a strong motivation for choosing the viscoelastic model rather than the Biot model for the inversion, provided, of course, that the viscoelastic model gives results similar to those of the Biot model.

The comparisons in Figs. 4 and 5 show that the viscoelastic model indeed gives rise to solutions quite close to those of the Biot model. This fact enabled us to choose the viscoelastic (rather than the Biot) model for the purpose of the inversions.

3.3. Method of solution of the inverse problem

As briefly mentioned above, the inversion proceeds in two distinct steps (actually three steps, because the density of the sample is first obtained from measurements of its geometry and weight).

The (real) elastic moduli E, ν are first retrieved by use of: (a) the data consisting of the experimentally observed resonance frequencies of the specimens vibrating under free–free boundary conditions, and (b) the elastic 3D FEM model (i.e., the viscoelastic model with no damping) to solve the eigenvalue problem via (2) (see, e.g., Ref. [38, pp. 570–500]) for the model values of the resonance frequencies associated with the trial values of E, ν at each iteration step during the inversion (see Fig. 6).

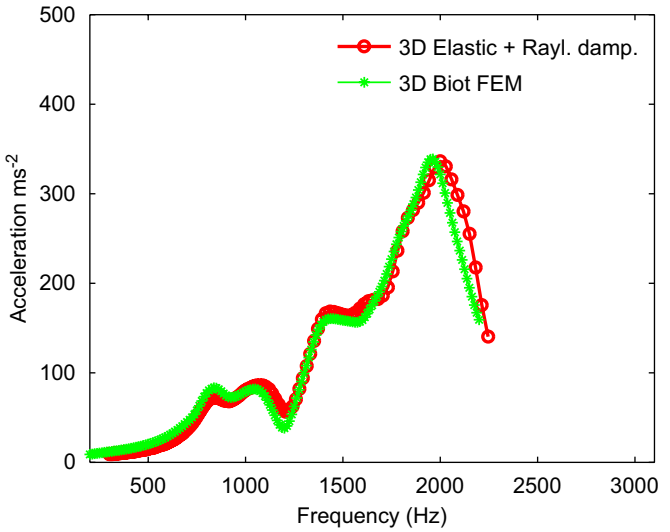

Fig. 5. Computed acceleration responses on a point of the surface of a 7 cm × 7 cm × 5 cm thick plate-like specimen to a harmonic point force applied at another point of the surface, obtained by: (i) the viscoelastic FEM model incorporating Rayleigh damping parameters $\alpha = 1200$ and $\beta = 5 \times 10^{-7}$ and (ii) the Biot FEM model.

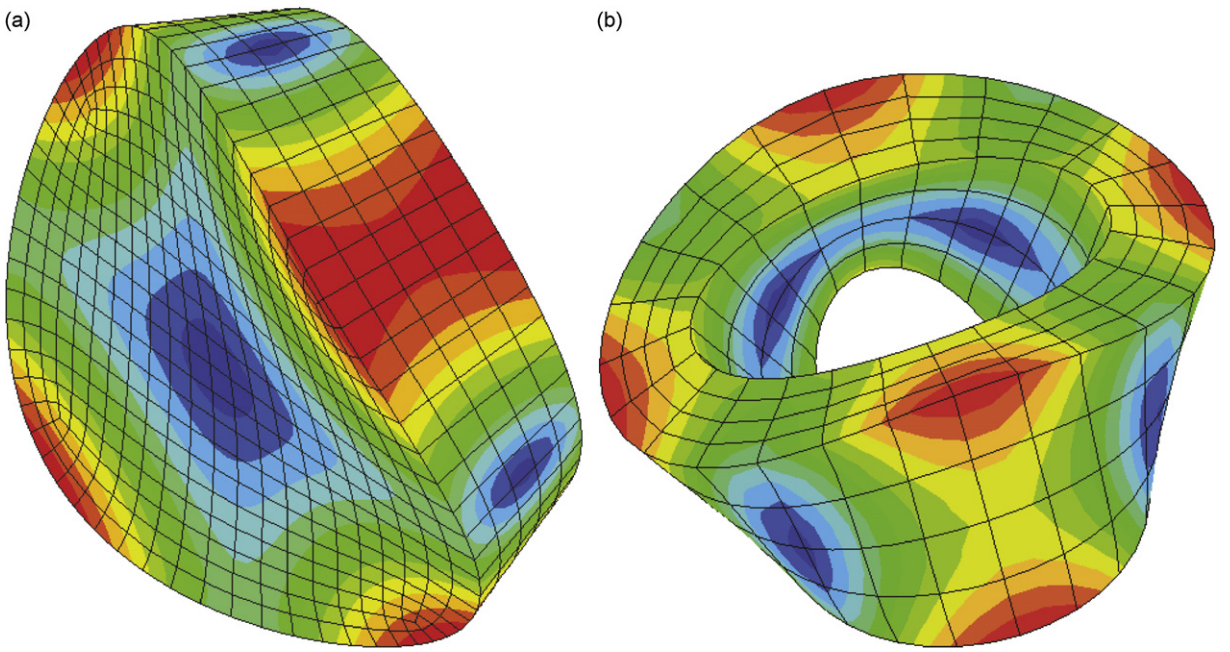

Fig. 6. The first mode shapes used in the inverse problem for the recovery of Young's modulus and Poisson ratio for (a) the thick melamine disc and (b) the hollow polyurethane cylinder.

A cost function $\mathfrak{J}$, constituting the measure of the discrepancy between the model resonance frequencies and the experimental resonance frequencies, is computed for each set of trial values of E, ν:

$$\mathfrak{J}(E,\nu) = \sum_{n=1}^{m} \mathfrak{w}_n^2 \{f^n_{\text{experiment}} - f^n_{\text{model}}(E,\nu)\}^2, \tag{7}$$

with ϖ_n being the weighting coefficient for the mode, $f^n_{\text{experiment}}$ the target resonance frequency obtained by experiment, n the mode number, m the number of employed modes and f^n_{model} the natural frequency furnished by the model for the current trial values of E and ν.

The search for the optimal set E, ν which minimizes $\Im$ is achieved automatically, and in an iterative manner, by the Levenberg–Marquardt optimization algorithm (i.e., the *lmdif* routine from *Minpack*, implemented in the Argonne National Laboratory).

The final step of the inversion procedure is to obtain the Rayleigh parameters α, β of the specimen by minimizing the discrepancy between the measured spectral responses and the responses computed by means of the viscoelastic model incorporating the previously obtained optimal set E, ν.

4. Results and discussion

4.1. Preliminaries

The vibration spectral response amplitudes and phases are first plotted for each specimen and the resonance frequencies are obtained by correlating the amplitude peaks to sudden phase variations.

These measured resonance frequencies are displayed in Table 2 for the various specimens under examination.

The elastic moduli and damping parameters are then retrieved by the procedure outlined in the previous section.

4.2. Particular aspects of the cost function

4.2.1. Uniqueness as manifested by a single minimum

Good practice for solving inverse problems requires that the recovered solution be unique. An indication of uniqueness can be found by plotting the cost functions, given by Eq. (7), as a function of the parameters one wishes to recover.

A cost function for PE1, computed with E in the range 140–200 kPa and the Poisson ratio in the range 0.0–0.5, when all the modes are attributed equal weights ($\varpi_n = 1$), is depicted in Fig. 7.

The noteworthy feature of this figure, typical of what occurs for all the specimens under examination, is that the solution is unique (the minimum of the cost function occurs at $E \sim 160$ kPa and $\nu \sim 0.4$).

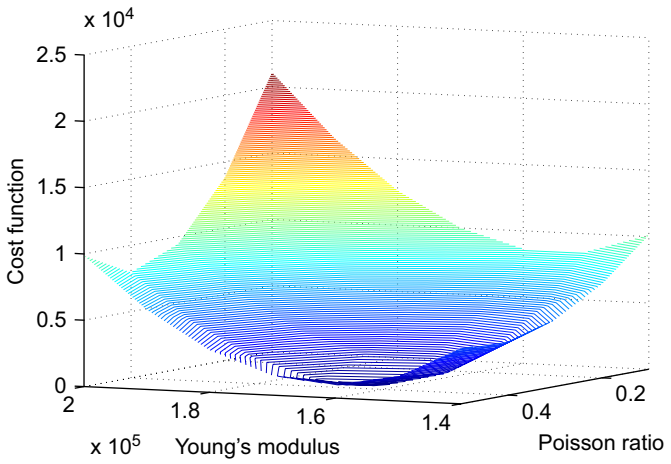

Fig. 7. The cost function to be minimized for the recovery of two variables (Young's modulus and the Poisson ratio for the melamine sample PE1) as a function of these variables.

4.2.2. Choice of weights

The resonance frequency of a natural mode may not be precisely determined for several reasons: mode-coupling, difficulties in distinguishing between the different types (compression, torsion and flexural) of modes and the presence of noise. In such cases it is best to assign weights and attribute the larger values to the more precisely determined natural frequencies. It is thus preferable to choose, if possible, the geometry of the specimen that will provide a vibration spectrum with well-separated resonance peaks.

4.2.3. Choice of the number of resonance frequencies

Increasing the number (larger m) of resonance frequencies in the cost function generally improves the rate of convergence of the inversion scheme. In practice, increasing m means including the higher vibrational modes. These modes are often more attenuated than the lower ones resulting in their peaks of resonance not being well marked. The mode density also increases with m such that some peaks of resonance become confounded and as a consequence become difficult to distinguish.

In Ref. [16], the accuracy of the reconstruction of the depth of the sea by echolocation was shown to depend on the sharpness of the cost function in the neighborhood of one of its minima. The sharpness was determined from the calculation of its absolute curvature.

Herein the slope of the cost function around the minima is analyzed. This can be illustrated by calculating the slope of $\Im$ with a fixed value of the Poisson ratio. In Ref. [33], the resonance frequencies (ω_n) obtained by solving an eigenvalue problem for thick elastic plates with varying diameter (R) and thickness (h) ratios are given in table form as a function of the non-dimensional frequencies $\lambda_n > 0$ with $\omega_n = (\lambda_n/R)\sqrt{E/(2\rho(1+v))}$. This is similar to the resonance frequencies of the Euler–Bernoulli beam model. The slope of the cost function using this model is given by

$$\frac{\mathrm{d}\Im(E)}{\mathrm{d}E} = \sum_{n=1}^{m} \frac{\lambda_n}{R}\sqrt{\frac{1}{2\rho(1+v)E}}(\omega_n - \omega_n^{\text{experiment}}), \tag{8}$$

when $(\omega_n - \omega_n^{\text{experiment}}) < 0$, the point is situated on the left side of the minimum of $\Im$ and the slope is negative, so that increasing the number of terms in the series increases the absolute value of the (negative) slope. A similar reasoning shows that when the point is on the right side of the minimum of $\Im$, increasing m increases the absolute value of the (positive) slope.

An illustration of this finding is given in Fig. 8 wherein the cost function is computed by varying Young's modulus with the Poisson ratio fixed at 0.4. This figure reveals that employing the largest (five) number of

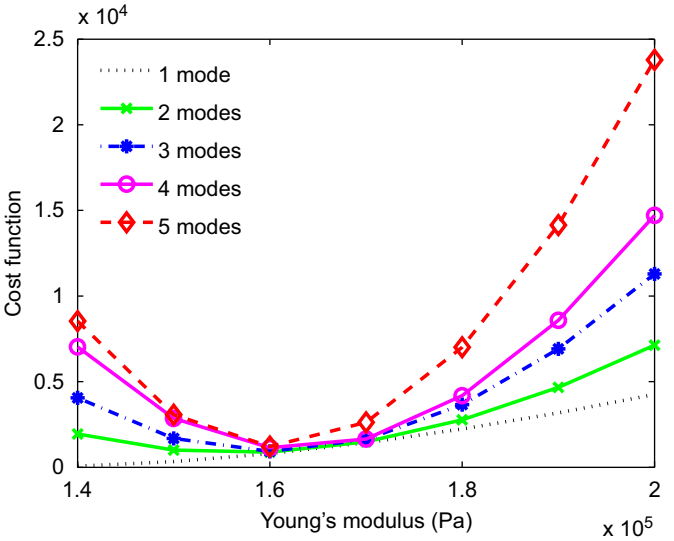

Fig. 8. The influence of the number of modes employed in the inversion scheme on the sharpness of the cost function for sample PE1.

modes for the inversion provides the sharpest minimum, thus allowing a faster convergence and a more precise solution of the inverse problem.

4.3. The outcome of the inversion scheme for samples PE1 and PE2

The recovered parameters, Young's modulus and Poisson ratio for the two melamine disc samples PE1, PE2 and the hollow polyurethane cylinder PE4, are given in Table 2.

4.4. Comparison between experimental and model responses for samples PE1 and PE2

Acceleration and strain were computed by the 3D viscoelastic FEM model employing the elastic moduli and damping factors obtained by the previously described inversion procedure. The computed strain (ε_{22}) is picked on a centroid of the element (this is an interpolation of integration point quantities to the centroid of an element). The position of the element corresponds to that of the measurement. The model and experimental responses are depicted in Fig. 9.

Table 2
Measured resonance frequencies (in Hz) and inversion results (the room temperature was 25 °C and the atmospheric pressure was 1.013×10^5 Pa during the experiment) compared to some reported values for samples PE1 and PE2

Sample	f^1_{exp}	f^2_{exp}	f^3_{exp}	f^4_{exp}	f^5_{exp}	f^6_{exp}	E	v	η_1	η_2
PE1	290	542	612	633	726	–	160	0.40	133	0.16
PE2	292	515	–	–		870	163	0.40		
PE3	–	–	–	–	–		160	0.40	133	0.12
PE4		341	680	850			911	0.28	2.3×10^3	13.7

The units of E are in kPa and those of viscosity (η_1 and η_2) are in $\mathrm{N\,m^{-2}s}$ (also termed Pascal seconds (Pa s)). In Ref. [43], $E = 160$ kPa, $v = 0.44$ for PE1, PE2 and PE3.

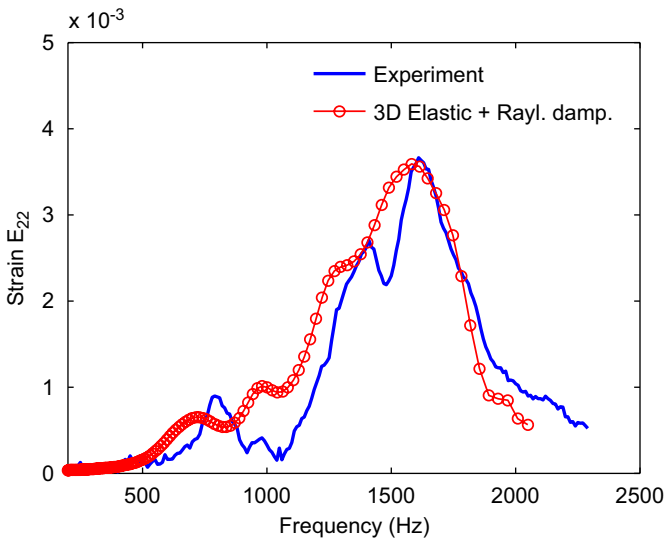

Fig. 9. Response of the melamine 2.5 cm thick disc. Comparison between the strain measured by the PZT sensor and the computed strain using the 3D viscoelastic FEM with Rayleigh damping. The Rayleigh damping parameters for this fit are $\alpha = 1200$ and $\beta = 1 \times 10^{-6}$.

4.5. The outcome of the inversion scheme for sample PE3

The recovered parameters, Young's modulus and Poisson ratio for the square melamine (7 cm × 7 cm × 5 cm) thick plate specimen (PE3) are given in Table 2.

The elastic moduli and Rayleigh damping parameters for the thick plate specimen are found to be approximately the same as those of the disc samples. This is consistent with the fact that all of these samples are made of the same material (melamine) and that the elastic moduli and damping parameters are inherent to the material and should not depend on the sample size and shape.

4.6. Comparison between experimental and model responses for sample PE3

The recovered elastic constants and Biot parameters were employed to compute the vibrational response of the square melamine (7 cm × 7 cm × 5 cm) thick plate specimen (PE3). This response is compared to the experimental response (actually, the average response of five such specimens) in Fig. 10.

4.7. The outcome of the inversion scheme for sample PE4

A different material (polyurethane) in the form of a hollow cylinder (specimen PE4, Fig. 11) was characterized in the same way as above.

The recovered parameters, Young's modulus and Poisson ratio, for this specimen are given in Table 2.

4.8. Comparison between experimental and model responses for sample PE4

In Fig. 12, we compare the measured response of the hollow cylinder specimen PE4 to the computed 3D FEM viscoelastic response (for $\alpha = 400$ and $\beta = 1.5 \times 10^{-5}$).

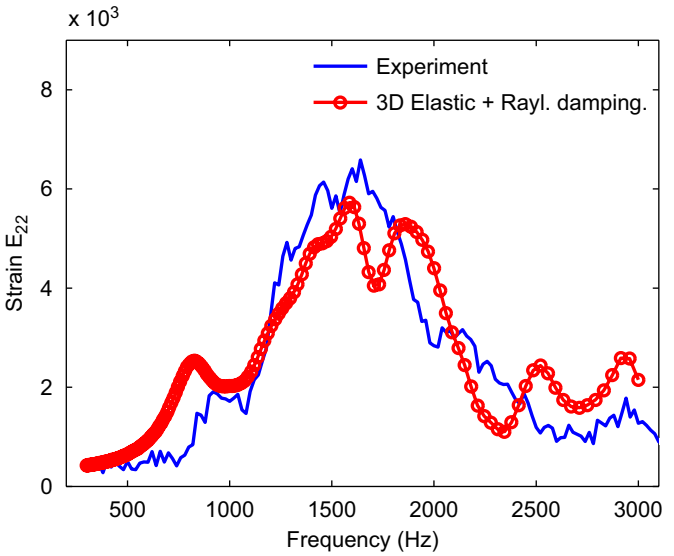

Fig. 10. Comparison between measured, averaged response of five quasi-identical PE3 (melamine (7 cm × 7 cm × 5 cm)) thick plate specimens with the computed viscoelastic FEM response (i.e., the strain ε_{22} on centroid of element at the measurement point). The computation is made with the Rayleigh damping parameters: $\alpha = 1200$, $\beta = 5 \times 10^{-7}$. The response is measured by a PZT sensor situated opposite the exciter as depicted in Fig. 1.

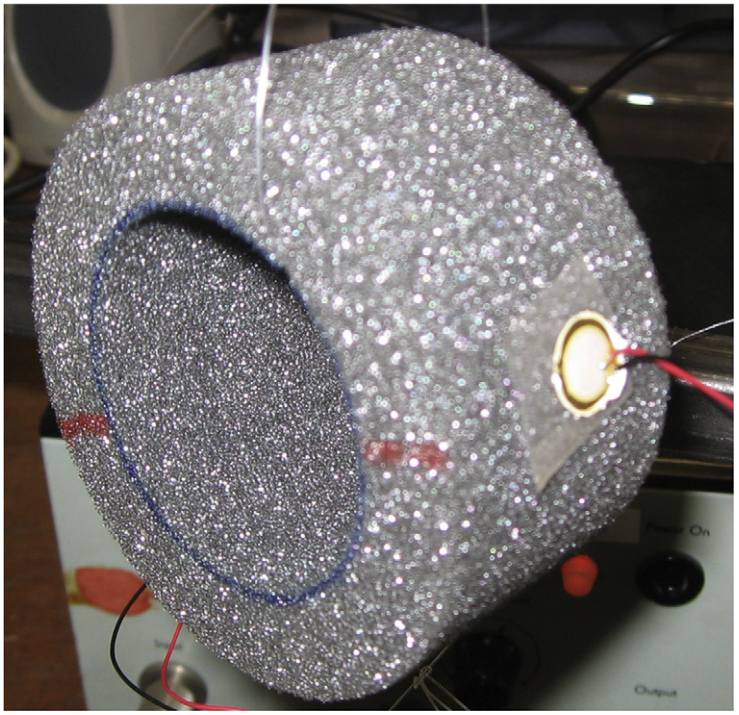

Fig. 11. Specimen PE4 (hollow polyurethane cylinder, exterior diameter 8 cm, longitudinal dimension 4.0 cm, thickness 1.5 cm) suspended by nylon threads. The PZT exciter (visible) and the sensor situated on the opposite side (not visible in the photograph) are mounted using a double-sided adhesive tape.

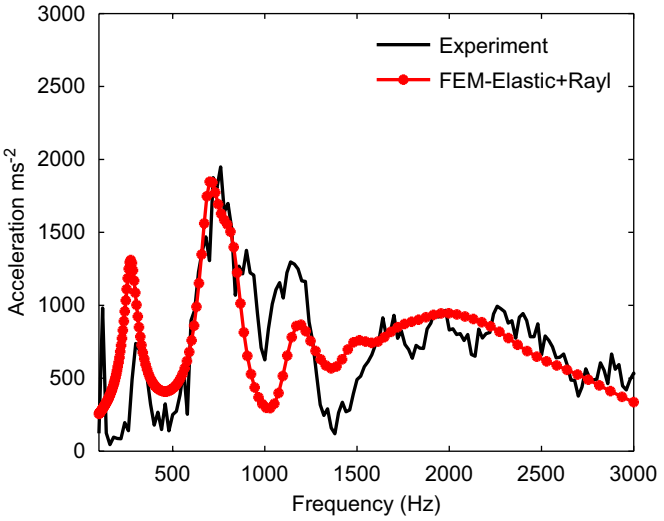

Fig. 12. Vibrational response of specimen PE4 (hollow polyurethane cylinder): comparison between the 3D viscoelastic FEM-computed (with $\alpha = 400$, $\beta = 1.5 \times 10^{-5}$) results and the experimental results.

4.9. *Quality and damping factors of melamine and polyurethane*

Using the previously mentioned inversion procedure of the measured response, we recovered the Rayleigh damping factors, and the variation of the attenuation factors with frequency, of the two cellular materials: melamine and polyurethane.

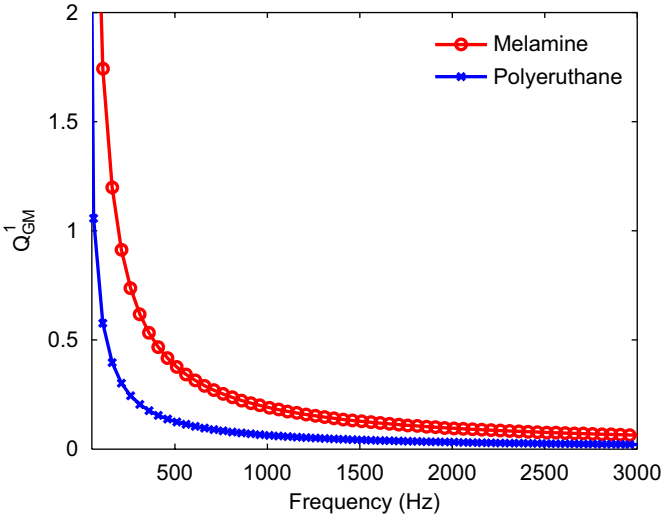

Fig. 13. Attenuation factor Q^{-1}_{GM} for melamine and polyurethane foams, resulting from the modified Maxwell model and the Rayleigh damping parameters α and β retrieved by inversion of experimental response. The system acts as a low-pass filter; the high-frequency modes dissipate almost completely.

The recovered modified Maxwell model parameters for the two materials are presented in Table 2, whereas Q^{-1}_{GM} is plotted in Fig. 13.

The comparison in Fig. 13 reveals that cellular melamine exhibits a larger attenuation than cellular polyurethane, particularly in the lower frequency range.

4.10. *Possible sources of errors in the determination of the material properties*

The major assumption made in this technique of recovery of the mechanical parameters is their non-frequency dependence in the frequency range studied. Measurement methods of the frequency dependence of dynamic Poissons ratio and loss factor can be found in Refs. [23,39,40].

4.10.1. *Anisotropy and geometric errors*

Natural cellular materials like bone and wood are anisotropic due to their weight-supporting nature.

Most foams are anisotropic to some extent due to the foaming process [8]. This is manifested in the resonance frequencies. The mechanical parameters used to compute these frequencies for the modes in the longitudinal direction will not give the correct values for the transverse and radial ones. A way to uncover anisotropy in the material is to compute the frequencies using an isotropic elastic model (e.g., for specimen PE4, which has been precisely cut by a machine), and then to compare the resonance frequencies for the breathing, radial, purely bending and longitudinal modes (here 820, 1091, 1387 and 2100 Hz, respectively). We have done this and found that these frequencies are very close if not equal to the measured ones (Table 2).

The thick disc-like specimens employed herein were cut using a cylindrical cutter made from a tin can (10 cm diameter). This simple tool can introduce some errors in the shape (supposed to be a thick circular plate or a thick disc in the computations) and lead to a poor determination of the volume and thus of the density of the material.

The solution of this problem is to scan the specimen with a laser to retrieve the exact geometry. Although this can solve the problem in the context of our inversion method, it does not solve the problem if the (disc-shaped) sample were to be characterized within a standing wave tube (due to the circumferential edge constraints entailed by the mounting conditions [41,42]). The acoustical measurements in the standing wave tube have been found to be less likely influenced by the edge constraints introduced by the mounting conditions if thin samples with an important diameter are used [41]. What may appear as effects due to

anisotropy can actually be caused by discrepancies between the actual specimen geometry and model geometry.

5. Conclusions

An experimental technique, employing a bonded (to the specimen) PZT exciter and sensor (which was shown to actually measure the strain at point), was developed to generate real data concerning the linear response to small-amplitude sinusoidal excitations of (e.g., cellular) materials that exhibit a nonlinear response even for moderate excitations.

An inversion procedure was described whereby the experimental linear response is compared to a model response in order to recover the homogenized elastic moduli and damping parameters of two types (melamine and polyurethane) of cellular materials.

The choice of the theory for computing the model response was shown to be a very important issue in that the model response is computed hundreds of times during the inversion. Ideally, the theory should incorporate all the important physics of the phenomena related to the generation of vibrations in the porous specimen. Although the Biot theory largely fulfills this role, it is very computationally intensive. We employed the Biot theory (implemented by our 3D FEM numerical code) to generate reference solutions whereby we evaluated another candidate theory. The latter is a classical one deriving from the elastodynamics of linear, isotropic, homogenized, elastic continua with the inclusion of Rayleigh damping (shown to be rheologically equivalent to a modified Maxwell model) to account for anelastic effects. This (viscoelastic) model was also translated into a 3D FEM numerical code which is far less time-consuming than the Biot model-based code. The results deriving from the two models were compared and shown to be quite similar, thus justifying the further use of the viscoelastic model in the inversion procedure.

The inverse problem of the retrieval of the elastic moduli and damping factors was then solved and shown to give rise to a unique solution (i.e., the cost function is convex and exhibits a single global minimum). Arguments were given, and results were shown, that indicate why it is advantageous to employ resonance frequency data for more modes in order to improve the precision and rate of convergence of the inversion. The sources of error, i.e., geometrical uncertainty and anisotropy of the specimens, of the recovered parameters were identified and discussed.

The transduction, measurement and inversion techniques developed herein for very low-amplitude excitations have thus been shown to enable the avoidance of the problems (i.e., recovered parameters that depend on the level of the excitation) encountered when the mechanical characteristics of materials, such as those of a cellular nature, are identified using vibrational response data that are clearly nonlinear even for moderate levels of excitation.

Appendix A. The steady-state linear dynamic equation

In the formulation of the steady-state linear dynamic analysis it is assumed that the structure undergoes small harmonic vibrations about a deformed, stress state defined by a subscript 0.

The procedure is to conform to the principle of virtual work

$$\int_{\Omega} \delta\underline{\underline{\varepsilon}}^{s} : \underline{\underline{\sigma}}^{s}\,\mathrm{d}\Omega + \int_{\Omega} \rho\delta\,\underline{u}\,.\ddot{\underline{u}}\,\mathrm{d}\Omega + \int_{\Omega} \rho a\delta\,\underline{u}\,.\dot{\underline{u}}\,\mathrm{d}\Omega - \int_{\partial\Omega} \delta\,\underline{u}\,.\,\underline{t}\,\mathrm{d}S = 0, \tag{A.1}$$

where a is the mass proportional damping factor, $\underline{t}$ the surface traction and $\delta\underline{\underline{\varepsilon}}^{s}$ the strain variation compatible with the displacement $\underline{u}$.

The discretized form of this equation is

$$\delta\underline{u}^{n}\{M^{nm}\ddot{\underline{u}}^{m} + (C^{nm}_{(M)}) + (C^{nm}_{(K)})\dot{\underline{u}}^{m} + K^{nm}\underline{u}^{m} - P^{n}\} = 0, \tag{A.2}$$

wherein:

- $M^{nm} = \int_{\Omega} \rho N^{n}.N^{m}\,\mathrm{d}\Omega$ is the mass matrix,
- $C^{nm}_{(M)} = \int_{\Omega} a\rho N^{n}.N^{m}\,\mathrm{d}\Omega$ is the mass damping matrix,

- $C^{nm}_{(K)} = \int_\Omega bB^n : D^{\mathrm{el}} : B^m \,\mathrm{d}\Omega$ is the stiffness damping matrix,
- $K^{nm} = \int_\Omega \left[\frac{\partial B^n}{\partial \underline{u}^m} : \underline{\sigma_0} + B^n : D^{el} : B^m\right] \mathrm{d}\Omega$ is the stiffness matrix,
- $P^n = \int_{\partial\Omega} N^n t \,\mathrm{d}S$ is the external load vector,
- D^{el} is the elasticity (moduli) matrix for the material,
- B is the strain variation matrix,
- b is the stiffness proportional damping factor and
- N^n and N^m are referred to as shape, basis or interpolating vector functions [38].

Appendix B. The modified Maxwell model

The stress–strain relationship for this model (Fig. 3) is given by

$$\sigma + \frac{\eta_1}{E}\frac{\partial\sigma}{\partial t} = (\eta_2 + \eta_1)\frac{\partial\varepsilon^s}{\partial t} + \frac{\eta_1\eta_2}{E}\frac{\partial^2\varepsilon^s}{\partial t^2}, \tag{B.1}$$

where E is the elasticity constant of the spring and η_1 and η_1 are the viscosities in the dashpots.

Taking periodic variations for the stress and strain ($\sigma(t) = \sigma_0 \exp(\mathrm{j}\omega t)$, $\varepsilon^s(t) = \varepsilon^s_0 \exp(\mathrm{j}\omega t)$), the complex modulus E_c is given by

$$E_c = \frac{\sigma_0}{\varepsilon^s_0} = \frac{-\eta_1\eta_2\omega^2 + \mathrm{j}E(\eta_2 + \eta_1)\omega}{(E + \mathrm{j}\eta_1\omega)}. \tag{B.2}$$

For weak-to-moderate Rayleigh damping, the dissipation factor Q^{-1} [31] and the damping ratio ξ are related by

$$Q^{-1} \approx 2\xi. \tag{B.3}$$

For a linear, viscoelastic rheological model of complex modulus $\mathbf{E}^* = \mathbf{E}_R + \mathrm{j}\mathbf{E}_I$, the expression of the quality factor is $Q = \mathbf{E}_R/\mathbf{E}_I$, and, for this particular generalized Maxwell model:

$$Q^{-1}_{\mathrm{GM}} = \frac{E(\eta_1 + \eta_2)}{\eta_1^2\omega} + \frac{\eta_2}{E}\omega. \tag{B.4}$$

The relationship between α and β and the mechanical parameters of the generalized Maxwell model is then given by

$$\alpha = E(\eta_1 + \eta_2)/\eta_1^2, \quad \beta = \frac{\eta_2}{E}. \tag{B.5}$$

Appendix C. Biot model

The porous media are coupled to a fluid and the displacement field is computed using the Biot theory formulated in the variables $\{\underline{u}, p\}$ ($\underline{u}$ being the mean displacement field of the frame and p the mean sound pressure in the fluid phase over a homogenization volume) by Atalla [35].

A variational formulation of the governing differential equations leads to:

$$\int_\Omega \hat{\underline{\underline{\sigma}}}^s(u) : \underline{\underline{\varepsilon}}^s(\delta\,\underline{u})\,\mathrm{d}\Omega - \omega^2\tilde{\rho}\int_\Omega \underline{u}.\delta\,\underline{u}\,\mathrm{d}\Omega - \tilde{\gamma}\int_\Omega \nabla p.\delta\,\underline{u}\,\mathrm{d}\Omega - \int_{\partial\Omega}[\hat{\underline{\underline{\sigma}}}^s.\underline{n}].\delta\,\underline{u}\,\mathrm{d}\Gamma = 0, \tag{C.1}$$

$$\frac{\phi^2}{\omega^2\tilde{\rho}_{22}}\int_\Omega \nabla p.\nabla\delta p\,\mathrm{d}\Omega - \frac{\phi^2}{\tilde{R}}\int_\Omega p\delta p\,\mathrm{d}\Omega - \tilde{\gamma}\int_\Omega \nabla\delta p.\,\underline{u}\,\mathrm{d}\Omega + \int_{\partial\Omega}\left[\tilde{\gamma}u_n - \frac{\phi^2}{\omega^2\tilde{\rho}_{22}}\frac{\partial p}{\partial n}\right]\delta p\,\mathrm{d}S = 0, \tag{C.2}$$

wherein:

- $\delta\,\underline{u}$ and δp denote admissible variations of $\underline{u}$ and p,
- $\underline{\underline{\varepsilon}}^s$ is the solid phase strain tensor,

- $\hat{\underline{\underline{\sigma}}}^s$ is the stress tensor of the solid phase of the material in the vacuum,
- $\tilde{\rho}$ and $\tilde{\rho}_{22}$ are the apparent densities of the solid and the fluid phases,
- $\tilde{\gamma}$ is a coupling factor between the two phases,
- $\widetilde{Q}$ and $\widetilde{R}$ are poroelastic coefficients whose expressions can be found in Ref. [35],
- Q and R are related to K_b, the bulk modulus of the frame *in vacuo*, to K_s, the bulk modulus of the elastic solid composing the frame, and to $\bar{K}_f$, the bulk modulus of the air in the pores,
- Ω stands for the porous material volume, $\partial\Omega$ denotes its boundary, subscript n denotes the normal component of a vector and $\underline{n}$ is the unit external normal vector of the boundary surface $\partial\Omega$.

References

[1] F. Bos, S. Bos Casagrande, Online non-destructive evaluation and control of wood-based panels by vibration analysis, *Journal of Sound and Vibration* 268 (2003) 403–412.

[2] P.S. Frederiksen, Estimation of elastic moduli in thick composite plates by inversion of vibrational data, in: H.D. Bui, M. Tanaka et al. (Eds.), *Inverse Problems in Engineering Mechanics*, Rotterdam, Balkema, 1994, pp. 111–118.

[3] X. Neil Dong, X. Edward Guo, The dependence of transversely isotropic elasticity of human femoral cortical bone on porosity, *Journal of Biomechanics* 37 (8) (2004) 1281–1287.

[4] B.J. Zadler, J.H.L. Le Rousseau, J.A. Scales, M.L. Smith, Resonant ultrasound spectroscopy: theory and application, *Geophysical Journal International* 156 (2004) 154–169.

[5] N. Sebaa, Z.E.A. Fellah, M. Fellah, E. Ogam, A. Wirgin, F.G. Mitri, C. Depollier, W. Lauriks, Ultrasonic characterization of human cancellous bone using the biot theory: inverse problem, *The Journal of the Acoustical Society of America* 120 (4) (2006) 1816–1824.

[6] T. Lee, R.S. Lakes, A. Lal, Resonant ultrasound spectroscopy for measurement of mechanical damping: comparison with broadband viscoelastic spectroscopy, *Review of Scientific Instruments* 71 (2000) 2855–2861.

[7] Y.C. Wang, R.S. Lakes, Resonant ultrasound spectroscopy in shear mode, *Review of Scientific Instruments* 74 (2003) 1371–1373.

[8] L.J. Gibson, M.F. Ashby, *Cellular Solids: Structure and Properties*, second ed., Cambridge Solid State Science, Cambridge University Press, Cambridge, 2001.

[9] M.A. Biot, Theory of propagation of elastic waves in a fluid-saturated porous solid. I. Low-frequency range, *Journal of the Acoustical Society of America* 28 (2) (1956) 168–178.

[10] M.A. Biot, Theory of propagation of elastic waves in a fluid-saturated porous solid. II. Higher frequency range, *Journal of the Acoustical Society of America* 28 (2) (1956) 179–191.

[11] Y. Champoux, J.F. Allard, Dynamic tortuosity and bulk modulus in air-satured porous media, *Journal of Applied Physics* 70 (4) (1991) 1975–1979.

[12] D.L. Johnson, J. Koplik, R. Dashen, Theory of dynamic permeability and tortuosity in fluid-saturated porous-media, *Journal of Fluid Mechanics* 176 (1987) 379–402.

[13] Keith Attenborough, Acoustical characteristics of rigid fibrous absorbents and granular materials, *The Journal of the Acoustical Society of America* 73 (3) (1983) 785–799.

[14] J.-F. Allard, C. Depollier, J. Nicolas, W. Lauriks, A. Cops, Proprietes acoustiques des materiaux poreux satures d'air et theorie de biot, *Journal of Acoustics* 3 (1990) 28–38.

[15] J.L. Buchanan, R.P. Gilbert, K. Khashanan, Determination of the parameters of cancellous bone using low frequency acoustic measurements, *Journal of Computational Acoustics* 12 (2004) 99–126.

[16] J. Buchanan, R. Gilbert, A. Wirgin, Y. Xu, Depth sounding: an illustration of some of the pitfalls of inverse scattering problems, *Mathematical and Computer Modelling* 35 (11–12) (2002) 315–1354.

[17] Z.E.A. Fellah, F.G. Mitri, M. Fellah, E. Ogam, A. Wirgin, W. Lauriks, C. Depollier, Ultrasonic characterization of porous absorbing materials: inverse problem, *Journal of Sound and Vibration* 302 (4–5) (2007) 746–759.

[18] M.A. Delany, E.N. Bazley, Acoustic properties of fibrous absorbent materials, *Applied Acoustics* 3 (1970) 105–l16.

[19] D.K. Wilson, Simple, relaxational models for the acoustical properties of porous media, *Applied Acoustics* 50 (3) (1997) 171–188.

[20] Z.E.A. Fellah, J.Y. Chapelon, S. Berger, W. Lauriks, C. Depollier, Ultrasonic wave propagation in human cancellous bone: application of biot theory, *The Journal of the Acoustical Society of America* 116 (1) (2004) 61–73.

[21] R.P. Gilbert, S. Zhang, E. Ogam, Y. Xu, *Determination of osteoporosis in a bone-muscle system*, Fifth International ISAAC Congress, Catania Italy, 2005.

[22] P. Leclaire, K.V. Horoshenkov, A. Cummings, Transverse vibrations of a thin rectangular porous plate saturated by a fluid, *Journal of Sound and Vibration* 247 (1) (2001) 1–18.

[23] M. Etchessahar, S. Sahraoui, L. Benyahia, J.F. Tassin, Frequency dependence of elastic properties of acoustic foams, *The Journal of the Acoustical Society of America* 117 (3) (2005) 1114–1121.

[24] C. Lang lois, R. Panneton, N. Atalla, Polynomial relations for quasi-static mechanical characterization of isotropic poroelastic materials, *The Journal of the Acoustical Society of America* 110 (6) (2001) 3032–3040.

[25] APCI, *Piezoelectric Ceramics: Principles and Applications*, American Piezo Ceramics, Inc., Mackeyville, PA, USA, 2004.

[26] M. Swaminadham, A. Santhanam, K. Pureswaran, J. Rao, Identification of resonant frequencies of rotating beams with the use of PZT crystals, *Experimental Mechanics* 19 (2) (1979) 76–80.

[27] J.D. McIntosh, R.F. Lambert, Nonlinear wave propagation through rigid porous materials. I: nonlinear parametrization and numerical solutions, *The Journal of the Acoustical Society of America* 88 (4) (1990) 1939–1949.
[28] D.K. Wilson, J.D. McIntosh, R.F. Lambert, Forchheimer-type nonlinearities for high-intensity propagation of pure tones in air-saturated porous media, *The Journal of the Acoustical Society of America* 84 (1) (1988) 350–359.
[29] E. Ogam, A. Wirgin, Z.E.A. Fellah, Y. Xu, Experimental and theoretical nonlinear dynamic response of intact and cracked bone-like specimens with various boundary conditions, *Journal of Vibration and Acoustics* 129 (5) (2007) 541–549.
[30] M. Liu, D.G. Gorman, Formulation of Rayleigh damping and its extensions, *Computers and Structures* 57 (2) (1995) 277–285.
[31] J.M. Carcione, *Wave Fields in Real Media: Wave Propagation in Anisotropic, Anelastic and Porous Media*, Pergamon, New York, USA, 2001.
[32] J.F. Semblat, Rheological interpretation of Rayleigh damping, *Journal of Sound and Vibration* 206 (5) (1997) 741–744.
[33] J. So, A.W. Leissa, Three-dimensional vibrations of thick circular and annular plates, *Journal of Sound and Vibration* 209 (1) (1998) 15–41.
[34] K.M. Liew, J.B. Han, Z.M. Xiao, Vibration analysis of circular mindlin plates using the differential quadrature method, *Journal of Sound and Vibration* 205 (5) (1997) 617–630.
[35] N. Atalla, R. Panneton, P. Deberge, A mixed pressure–displacement formulation for poroelastic materials, *Journal of the Acoustical Society of America* 104 (3) (1998) 1444–1542.
[36] Z.E.A. Fellah, S. Berger, W. Lauriks, C. Depollier, C. Aristegui, J.-Y. Chapelon, Measuring the porosity and the tortuosity of porous materials via reflected waves at oblique incidence, *The Journal of the Acoustical Society of America* 113 (5) (2003) 2424–2433.
[37] Karlsson & Sorensen Inc. Hibbitt., *Abaqus Standard User's Manual*, Vol. I. Pawtucket RI, v6.2 edition, 2001.
[38] T.J.R. Hughes, *Finite Element Method—Linear Static and Dynamic Finite Element Analysis*, Prentice–Hall, Englewood Cliffs, 2000.
[39] T. Pritz, Frequency dependences of complex moduli and complex poisson's ratio of real solid materials, *Journal of Sound and Vibration* 214 (1) (1998) 83–104.
[40] T. Pritz, Measurement methods of complex poisson's ratio of viscoelastic materials, *Applied Acoustics* 60 (2000) 279–292.
[41] D. Pilon, R. Panneton, F. Sgard, Behavioral criterion quantifying the edge-constrained effects on foams in the standing wave tube, *The Journal of the Acoustical Society of America* 114 (4) (2003) 1980–1987.
[42] D. Pilon, R. Panneton, F. Sgard, Behavioral criterion quantifying the effects of circumferential air gaps on porous materials in the standing wave tube, *The Journal of the Acoustical Society of America* 116 (1) (2004) 344–356.
[43] L. Jaouen, B. Brouard, N. Atalla, C. Langlois, A simplified numerical model for a plate backed by a thin foam layer in the low frequency range, *Journal of Sound and Vibration* 280 (3–5) (2005) 681–698.